The Astrophysical Journal, 730:79 (11pp), 2011 April 1 doi:10.1088/0004-637X/730/2/79

LHS 6343 C: A TRANSITING FIELD BROWN DWARF DISCOVERED BY THE *KEPLER* MISSION*

John Asher Johnson[1,2], Kevin Apps[3], J. Zachary Gazak[4], Justin R. Crepp[1], Ian J. Crossfield[5], Andrew W. Howard[6], Geoff W. Marcy[6], Timothy D. Morton[1], Carly Chubak[6], and Howard Isaacson[6]
[1] Department of Astrophysics, California Institute of Technology, MC 249-17, Pasadena, CA 91125, USA; johnjohn@astro.caltech.edu
[2] NASA Exoplanet Science Institute (NExScI), CIT Mail Code 100-22, 770 South Wilson Avenue, Pasadena, CA 91125, USA
[3] Cheyne Walk Observatory, 75B Cheyne Walk, Horley, Surrey, RH6 7LR, UK
[4] Institute for Astronomy, University of Hawai'i, 2680 Woodlawn Drive, Honolulu, HI 96822, USA
[5] Department of Physics and Astronomy, University of California Los Angeles, Los Angeles, CA 90095, USA
[6] Department of Astronomy, University of California, Mail Code 3411, Berkeley, CA 94720, USA
Received 2010 September 8; accepted 2011 January 18; published 2011 March 8

ABSTRACT

We report the discovery of a brown dwarf that transits one member of the M+M binary system LHS 6343 AB every 12.71 days. The transits were discovered using photometric data from the *Kepler* public data release. The LHS 6343 stellar system was previously identified as a single high proper motion M dwarf. We use adaptive optics imaging to resolve the system into two low-mass stars with masses $0.370 \pm 0.009\ M_{\odot}$ and $0.30 \pm 0.01\ M_{\odot}$, respectively, and a projected separation of 0.″55. High-resolution spectroscopy shows that the more massive component undergoes Doppler variations consistent with Keplerian motion, with a period equal to the transit period and an amplitude consistent with a companion mass of $M_C = 62.7 \pm 2.4\ M_{\rm Jup}$. Based on our analysis of the transit light curve, we estimate the radius of the companion to be $R_C = 0.833 \pm 0.021\ R_{\rm Jup}$, which is consistent with theoretical predictions of the radius of a >1 Gyr brown dwarf.

Key words: binaries: eclipsing – binaries: spectroscopic – brown dwarfs – stars: fundamental parameters – stars: low-mass – techniques: photometric – techniques: radial velocities

Online-only material: color figures

1. INTRODUCTION

Situated on the mass continuum between planets and hydrogen-burning stars are objects commonly known as brown dwarfs, with masses spanning approximately 13 $M_{\rm Jup}$ up to 80 $M_{\rm Jup}$ (assuming solar metallicity). Since the first discoveries of these substellar objects 15 years ago (Oppenheimer et al. 1995; Basri et al. 1996), various surveys have found additional examples in numbers exceeding the population of known exoplanets.[7] However, despite the large sample of brown dwarfs, very little is known about the physical properties or formation mechanism(s) of these substellar objects (e.g., Basri 2006; Burgasser et al. 2007; Liu et al. 2008).

Most known brown dwarfs have been discovered as solitary objects by wide-field, near-infrared (NIR) imaging surveys (e.g., Martin et al. 1997; Burgasser et al. 1999; Lawrence et al. 2007; Delorme et al. 2008). Their identification is often based on spectral typing, with physical parameters derived from comparing photometric measurements to substellar evolutionary models. Knowledge beyond spectral typing is limited by the difficulty in modeling the complex molecular features that dominate the spectra of cool dwarfs (e.g., Allard et al. 2001; Cushing & Vacca 2006), a problem that persists above the hydrogen-burning mass limit for M-type dwarfs (Maness et al. 2007; Johnson & Apps 2009).

The preferred method of measuring physical properties of substellar objects such as masses, compositions, and ages is to study examples that are physically associated with brighter main-sequence stars. By assuming that both the brown dwarf and its host star formed at the same time from the same molecular cloud, ages and chemical composition of the companion can be tied to the properties of the brighter, more easily characterized component (Liu & Leggett 2005; Bowler et al. 2009). However, brown dwarfs in these favorable "benchmark" configurations are found in numbers far below the sample of exoplanets, despite their relative ease of detection compared to planet-mass companions. This observed feature of the substellar mass distribution of bound companions is known as the "brown dwarf desert," and the barren region extends over a wide swath around stars, extending from ≈0.05 AU out to hundreds of AU (Marcy & Butler 2000; McCarthy & Zuckerman 2004; Grether & Lineweaver 2006; Johnson 2009).

The existence of a deep minimum in the mass continuum between stars and planets suggests that distinct formation mechanisms operate at either mass extreme, one for stellar objects and one for planets. However, the scarcity of objects in the brown dwarf desert makes it difficult to determine where this line should be drawn. For example, it is unclear whether a 20 $M_{\rm Jup}$ object in orbit around a main-sequence star formed like a massive planet or instead should be considered part of the extreme low-mass tail of the stellar initial mass function (Kratter et al. 2010). Furthermore, an issue as fundamental as the mass–radius relationship below the hydrogen-burning limit, is largely unconstrained by observations. Understanding the nature and origins of brown dwarfs requires a much larger sample of detections.

One promising avenue for increasing the sample of well-characterized substellar companions is through wide-field photometric transit surveys. Since the radii of objects are roughly constant from 1 to 100 $M_{\rm Jup}$ (Baraffe et al. 1998), transit surveys are uniformly sensitive to companions throughout the entire

* Based on observations obtained at the W. M. Keck Observatory, which is operated jointly by the University of California and the California Institute of Technology. Keck time has been granted by Caltech, the University of California, and NASA.
[7] http://spider.ipac.caltech.edu/staff/davy/ARCHIVE/index.shtml

brown dwarf desert. The transit light curve, together with precise radial velocities (RVs), provide both the absolute mass (as opposed to minimum mass, $M \sin i$) and radius of the companion, thereby directly testing the predictions of interior structure models (Burrows et al. 1997; Torres et al. 2008). Once transits have been discovered, the door has opened up a wealth of follow-up opportunities that can measure properties such as the brown dwarf's albedo, temperature distribution, emission spectrum, and atmospheric composition (see, e.g., the review by Charbonneau et al. 2005). Further, studying the distribution of physical characteristics of companions, and their relationships to the characteristics of their host stars, can inform theories of the origins of brown dwarfs in the same way that the statistical properties of exoplanets inform theories of planet formation (Fischer & Valenti 2005; Torres et al. 2008; Johnson et al. 2010).

In this contribution, we present the discovery and characterization of a transiting brown dwarf orbiting a nearby low-mass star in the *Kepler* field.

2. PHOTOMETRIC OBSERVATIONS

2.1. Kepler Photometry

The *Kepler* space telescope is conducting a continuous photometric monitoring campaign of a target field near the constellations Cygnus and Lyra. A 0.95 m aperture Schmidt telescope feeds a mosaic CCD photometer with a $10^\circ \times 10^\circ$ field of view (Koch et al. 2010; Borucki et al. 2010). Data reduction and analysis is described in Jenkins et al. (2010b) and Jenkins et al. (2010c), and the photometric and astrometric data were made publicly available as part of the first-quarter (Q0–Q1) data release. We downloaded the data from the Multimission Archive at STScI, and we use the pipeline-corrected light curves. The Q0 data have a time baseline UT 2009 May 5–11, and the Q1 data span UT 2009 May 13 through 2009 June 16.

Among the 156,000 Long Cadence stellar targets in the *Kepler* field is the nearby, high proper motion M dwarf LHS 6343 ($\alpha = 19^{\rm h}10^{\rm m}14\overset{\rm s}{.}31$, $\delta = +46^\circ57^{\rm m}25\overset{\rm s}{.}0$; Reid et al. 2004). The photometric properties as listed in the Kepler Input Catalog (KIC; Batalha et al. 2010) are given in Table 1. The Q0–Q1 photometric time series of LHS 6343 contains a total of 2115 brightness measurements with a 29.4 minute cadence and a median internal measurement precision of 7×10^{-5} (Jenkins et al. 2010c).

As part of a study of the photometric variability of the closest stars in the *Kepler* field, one of us (K.A.) noted that the light curve of LHS 6343 exhibits four deep, periodic dimming events spaced by 12.71 days. The light curve depths are constant to 0.3 mmag and exhibit no obvious additional dimming at intermediate periods, consistent with the signal of a transiting planet-sized object. The astrometry shows no shift in the center of light greater than 1 millipixel (4 mas; Jenkins et al. 2010a), and there are no secondary eclipses evident at intermediate phases. It is therefore unlikely that the source of the dimming events is a background eclipsing binary (EB).

Examination of the Palomar Observatory Sky Survey (POSS) images shows no other stars at the current position of LHS 6343, further ruling false-positives involving an EB. The closest star in the archival images is $7\overset{''}{.}0$ to the west of LHS 6343, near the edge of the *Kepler* photometric aperture. However, the star is only 4% as bright as LHS 6343, meaning that if it is an EB, it would have to nearly disappear to replicate the observed transit signal. This situation is ruled out by the lack of a large photocenter shift seen in the astrometric measurements. The *Kepler* photometric measurements phased at the 12.71 day period are shown in Figure 1.

Table 1
Observed Properties of LHS 6343

Parameter	Value	Source
α	19 10 14.33	KIC
δ	+46 57 25.5	KIC
μ_α (mas yr^{-1})	−145	KIC
μ_δ (mas yr^{-1})	−401	KIC
g'	14.03 ± 0.02	KIC
r'	13.06 ± 0.02	KIC
i'	12.07 ± 0.02	KIC
$B_{\rm tot}$	15.009 ± 0.025	
$V_{\rm tot}$	13.435 ± 0.018	
$K_{P,{\rm tot}}$	13.104 ± 0.04	KIC
$J_{\rm tot}$	9.570 ± 0.021	2MASS
$H_{\rm tot}$	8.972 ± 0.027	2MASS
$K_{S,{\rm tot}}$	8.695 ± 0.011	2MASS
ΔJ	0.49 ± 0.05	PHARO
ΔH	0.48 ± 0.05	PHARO
ΔK_S	0.45 ± 0.06	PHARO
J_A	10.10 ± 0.04	
J_B	10.59 ± 0.06	
H_A	9.51 ± 0.04	
H_B	9.99 ± 0.07	
$K_{S,A}$	9.25 ± 0.05	
$K_{S,B}$	9.70 ± 0.08	

2.2. Nickel Z-band Photometry

We observed the transit event predicted to occur on UT 2010 June 29 using the 1 m Nickel telescope at Lick Observatory on Mt. Hamilton, California. We used the Nickel Direct Imaging Camera, which uses a thinned Loral 2048^2 pixel CCD with a $6\overset{'}{.}3$ square field of view (Johnson et al. 2008). We observed through a Gunn Z filter, used 2×2 binning for an effective pixel scale of $0\overset{''}{.}37$ pixel^{-1}, and a constant exposure time of 75 s. We used the slow readout mode, with 34 s between exposures to read the full frame and reset the detector. The conditions were clear with $\sim 1\overset{''}{.}0$ seeing. We began observing as soon as possible after sunset at an airmass of 1.4 and observed continuously for 5.4 hr bracketing the predicted transit midpoint, ending at an airmass of 1.05.

We measured the instrumental magnitude of LHS 6343 with respect to the four brightest comparison stars in the field using an aperture width of 23 pixels and a sky annulus with an inner and an outer radius of 28 and 33 pixels, respectively. We converted the Nickel timestamps to $\rm BJD_{UTC}$ using the techniques of Eastman et al. (2010) to be consistent with the *Kepler* data. The Nickel photometric measurements phased at the 12.71 day period are shown in Figure 1.

2.3. Johnson BV Photometry from HAO

The blended light of the stellar binary was observed in the Johnson B and V bands under photometric conditions by the privately owned Hereford Arizona Observatory (HAO) 11 inch telescope on 2010 August 31 and 2010 September 1, together with a program of standards from Landolt (1992). This telescope is equipped with a 1.5 k×1 k CCD with a plate scale of $0\overset{''}{.}81$ pixel^{-1}. For each program night, the standard star instrumental magnitudes were fit with a generic photometric equation (see Gary 2007 for more information on calibration procedures at HAO), and the resulting fit used to calculate the

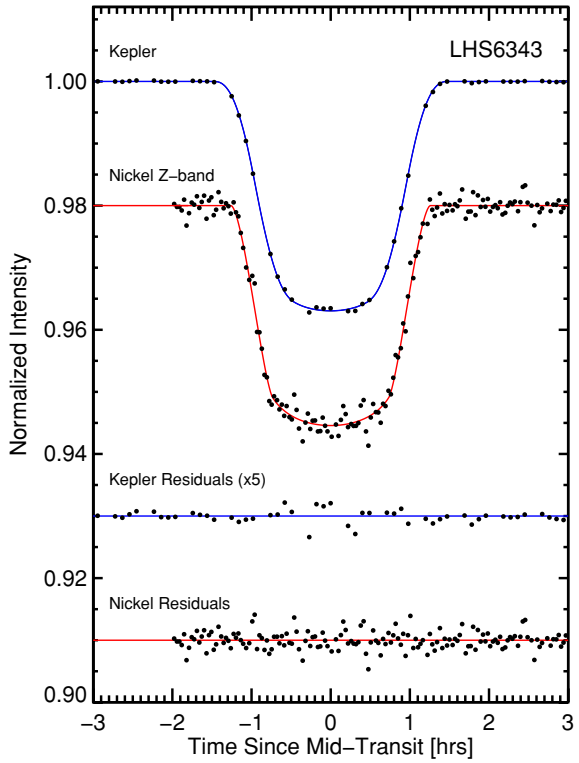

Figure 1. *Kepler* (blue) and Nickel (red) light curves, phased at the photometric period. The best-fitting light curve models are shown for each data set (see Section 5.3), and the residuals are shown beneath each light curve. The *Kepler* residuals have been multiplied ×5 for clarity.

(A color version of this figure is available in the online journal.)

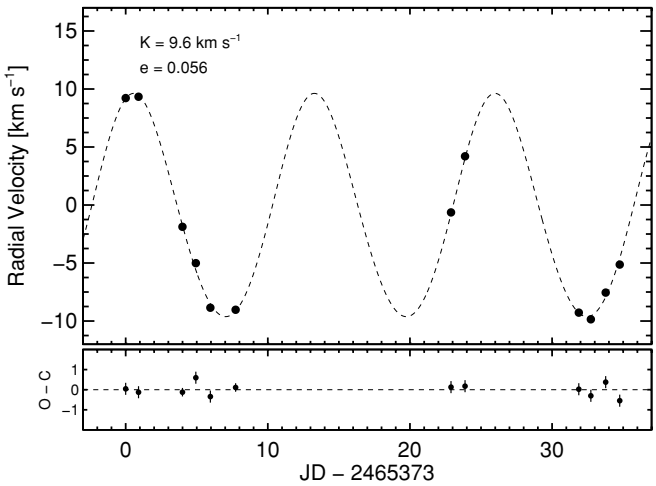

Figure 2. Keck/HIRES radial velocity measurements of LHS 6343 A. The best-fitting Keplerian orbit solution is shown as a dashed line. The systemic velocity, $\gamma = -46.0 \pm 0.2$ km s^{-1}, has been subtracted for clarity. The lower panel shows the RV residuals about the best-fitting orbit.

apparent magnitudes of LHS 6343. The set of standard stars were well behaved and there was no evidence of clouds or changes in extinction during the night. However, the magnitudes were corrected for flux from a nearby faint target 7″ from the main object. The corrections were small (0.128 ± 0.005 and 0.067 ± 0.003). The calibrated magnitudes obtained on the two nights were averaged together to derive the final values. The variation of the independently determined measurements obtained on the two nights was <0.01 mag in both *B* and *V*. The final values of $B_{\rm tot}$ and $V_{\rm tot}$ are given in Table 1.

3. RADIAL VELOCITIES AND ORBIT SOLUTION

We obtained spectroscopic observations of LHS 6343 at Keck Observatory using the HIgh Resolution Echelle Spectromter (HIRES) with a resolution of $R \approx 55{,}000$, with the standard iodine-cell setup used by the California Planet Survey (Howard et al. 2010). The transit depth, together with a rough stellar radius estimate of 0.4 $R_\odot$, appeared consistent with a planet with a radius of $\sim$0.7 $R_{\rm Jup}$. In anticipation of a low-amplitude Doppler signal, we initially used 45 minute exposures through the iodine cell and C2 decker for sky-subtraction. The resulting signal-to-noise ratio was ≈120 at 6300 Å. The wavelength coverage of our HIRES setup encompasses both the lithium line near 6708 Å, which shows no significant detection, as well as the Hα which is seen in absorption, ruling out extreme youth for the LHS 6343 system.

A cross-correlation analysis of the first two observations revealed two peaks separated by $\sim$10 km s^{-1}. The lack of a coincident background star in the POSS images suggests that the second set of lines must be from a physically associated binary companion and that LHS 6343 is a double-lined spectroscopic binary. Adaptive optics observations described in Section 4 confirmed the existence of a wide binary companion at a projected separation of 0.″55. Hereafter, we refer to the more massive component as Star A, and the less massive component as Star B.

In order to discern which component of the binary system is transited by a companion, we made subsequent HIRES observations with a position angle oriented along the binary axis to ensure the light from both stars fell within the slit. The cross-correlation analysis of the third observed spectrum revealed that the deeper set of absorption lines shifted by $\sim$10 km s^{-1} with respect to the first observation, indicating that Star A is orbited by a massive companion.

Our remaining HIRES spectra were obtained without the iodine cell and with 3 minute exposure times. We measured the RV of Star A using the cross-correlation analysis described by Johnson et al. (2004). However, we modified the procedure by constructing a double-lined cross-correlation template. We began with an iodine-free spectrum of the HD 265866 (M3V) for Star A and added to this template a scaled, shifted version of itself to represent the spectrum of Star B. For each observation, we adjusted the scaling and Doppler shift of spectrum B with respect to spectrum A until the cross-correlation peak was maximized. We then measured the centroid of the optimized cross-correlation function by fitting a parabola to the region near the resulting single peak.

We corrected for shifts in the HIRES detector by using the telluric lines in the 630 nm α-band as a wavelength reference. We measured the absolute RVs of LHS 6343 A with respect to the absolute RV of HD 265866 (M3V; $V_r = +22.97 \pm 0.50$ km s^{-1}; Chubak & Marcy 2011), and the resulting RV is corrected to the solar system barycenter using the velocity corrections computed by the CPS data reduction pipeline. The full time series of RV measurements is displayed in Figure 2. The RVs are also listed in Table 2, along with the heliocentric Julian Dates of observation and internal measurement errors.

We searched for the best-fitting Keplerian orbit solution using the partially linearized, least-squares fitting procedure described in Wright & Howard (2009) and implemented in the

Table 2
Radial Velocities for LHS 6343

JD −2440000	RV (km s^{-1})	Uncertainty (km s^{-1})
15373.095	−38.40	0.21
15373.998	−37.51	0.17
15377.078	−49.42	0.50
15377.099	−49.56	0.45
15378.030	−52.56	0.41
15379.052	−56.39	0.44
15380.827	−55.83	0.48
15380.831	−54.84	0.47
15395.983	−47.92	0.57
15396.970	−42.63	0.51
15404.974	−55.90	0.59
15405.821	−56.32	0.46
15406.865	−53.69	0.51
15407.854	−51.31	0.57

IDL software package RVLIN[8]. We fixed the period and mid-transit time based on the light curve analysis in Section 5.3, which leaves only four free parameters in our Keplerian model: the velocity semiamplitude (K_A), argument of periastron (ω), systemic velocity, (γ) and eccentricity. We find that the RVs are described well by a nearly circular orbit ($e = 0.056 \pm 0.032$) with a velocity semiamplitude $K = 9.6 \pm 0.3$ km s^{-1}. The full spectroscopic orbit is given in Table 5 and shown in Figure 2.

The parameter uncertainties were estimated using a bootstrap Monte Carlo algorithm. For each of 5000 realizations of the data, the measured RVs are perturbed by adding residuals randomly drawn from about the best-fitting orbital solution, with replacement. We chose this technique over a Markov Chain Monte Carlo (MCMC) analysis out of concern that our RV measurement uncertainty is dominated by systematic errors related to imperfect treatment of the second set of absorption lines, rather than photon noise. Thus, instead of assuming that the RVs are normally distributed about the model, we use the residuals themselves as an estimate of the noise model.

4. PALOMAR ADAPTIVE OPTICS IMAGING

We acquired near-infrared images of LHS 6343 on UT 2010 June 29 using the Palomar 200 inch telescope adaptive optics system and PHARO camera (Hayward et al. 2001; Troy et al. 2000). These diffraction-limited observations spatially resolve the target into a binary, as shown in Figure 3. We used these observations to calculate the relative brightness of each component of the visual binary and to subsequently constrain the range of possible masses (see Section 5). Our results for differential magnitudes in each of the J, H, K_S filters are listed in Table 1.

We used aperture photometry to measure the differential magnitudes of the two stars. However, given their relatively small angular separation, special care was taken to account for cross-contamination between the components. To remove the majority of flux contributed by the neighboring star, we used the spatial symmetry in the images. The amount of contaminating starlight was estimated by summing the counts over a region the same size as the photometric aperture located on the side opposite the star of interest.

Once the contaminating light from the neighboring star is removed, we find that the photometric precision is limited to several percent by uncertainties resulting from the subtraction residuals, as well as CCD nonlinearity and point-spread function (PSF) centroiding. These error sources contribute similarly to the overall uncertainty and were added in quadrature, neglecting any correlations between PSF centroiding errors and contamination removal, which we found to be comparatively small. To this, we also added in quadrature the standard deviation in the mean flux ratio of the companions over the 20 images acquired in each bandpass. Observations in the K_S band have a slightly larger uncertainty than in J and H, since the binary separation subtends a smaller angle on the sky in units of resolution elements.

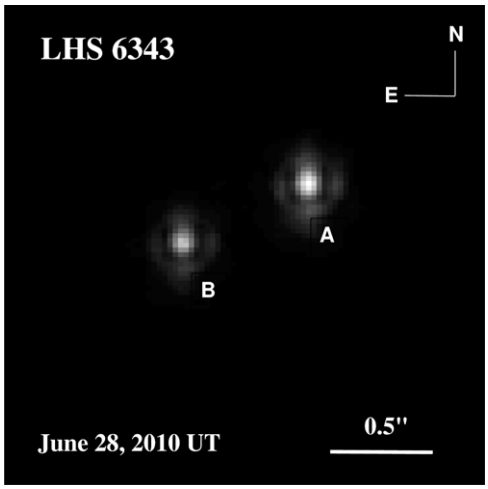

Figure 3. PHARO K_S-band adaptive optics image of LHS 6343 showing the two M-type components of the system. Star A is to the upper right of the image and Star B is to the lower left.

5. STELLAR PROPERTIES

The physical properties of the two stellar components of the wide binary, hereafter Star A and Star B, are of central importance to measuring the properties of the substellar companion, LHS 6343 C. The mass of the companion is related to the mass of Star A (M_A) and the companion's radius depends on the stellar radius, R_A. The luminosity of Star B is also important for the measurement of the companion's radius, as its contribution to the total flux of the system dilutes the transit depth. In fact, for the specific case of LHS 6343 the precision with which we can measure the companion radius will depend critically on our estimate of the "third light" contribution of Star B, rather than the photometric precision of the transit light curve (Irwin et al. 2010).

Because low-mass stars spend nearly their entire lives close to the zero-age main sequence, their observed properties are a function of two physical characteristics: mass and, to a lesser extent, metallicity. There are two widely used methods estimating the masses of M dwarfs. The first involves a comparison of observed properties such as absolute magnitude and color index, or luminosity and effective temperature, to tabulated stellar evolution models, such as those calculated by Baraffe et al. (1998). However, studies of low-mass EBs have demonstrated that these models systematically underpredict stellar radii (Ribas 2006; López-Morales 2007), even in cases when stellar activity should play a minimal role in shaping stellar structure (Torres 2007).

The other method makes use of empirical relationship between the near-infrared luminosity of a star and its mass, as

[8] http://exoplanets.org/code/

parameterized by Delfosse et al. (2000). We use the empirical relationships almost exclusively in order to avoid any systematic errors in the stellar evolution models. However, since the mass–luminosity relationships require absolute magnitudes, the distance to the star must be known to accurately estimate the stellar mass. Unfortunately, there is no published trigonometric parallax for LHS 6343, and the spectroscopic parallax of Reid et al. (2004) is unreliable because it is based on the total magnitude and colors of the binary system rather than the individual stars.

While the binarity of LHS 6343 in some regards poses a challenge, having two stars with the same age and chemical composition, together with the available photometric measurements, provides a unique opportunity to determine the physical characteristics of the two components. As we will demonstrate, the luminosity difference between the two stars constrains the mass ratio, while the total luminosity constrains the total mass, distance, and metallicity of the system.

An additional constraint on the mass is provided by the shape of the transit light curve. The slope of the ingress/egress yields the scaled semimajor axis $a/R_A \equiv a_R$, which is related to the density of Star A through Kepler's third law (e.g., Seager & Mallén-Ornelas 2003; Sozzetti et al. 2007; Winn 2008). However, the true value of a_R depends on the true transit depth $(R_C/R_A)^2$, which in turn is related to the amount of dilution in the light curve due to Star B.

In what follows, we first relate the masses of Star A and Star B to the available observables. We then estimate the flux contribution of Star B in the *Kepler* bandpass, which provides a refined estimate of the stellar masses. The iteration of this procedure yields the stellar parameters of Star A, which allows us to estimate the physical characteristics of the transiting object LHS 6343 C.

5.1. Stellar Masses

The most useful data available to us comprise seven photometric measurements: the total near-infrared magnitudes in the 2MASS catalog denoted by $\mathcal{T}_i$, where $i = J, H, K_S$ corresponds to the three bands, respectively; the magnitude differences $\Delta J, \Delta H, \Delta K_S$ from our AO imaging, denoted by Δ_i. We also have the total Johnson V- and B-band magnitudes $V_{\rm tot} = 13.435 \pm 0.018$ and $B_{\rm tot} = 15.009 \pm 0.025$. Our $V_{\rm tot}$ agrees well with the value listed in the two-armed spiral shock catalog, $V_{\rm tot} = 13.38 \pm 0.24$ (Droege et al. 2006). These magnitudes yield the system color $(B-V)_{\rm tot} = 1.574 \pm 0.031$.

The individual apparent magnitudes in the ith NIR band (JHK) of Star A ($m_{i,A}$) and Star B ($m_{i,B}$) are related to the total magnitudes $\mathcal{T}_i$ and magnitude differences Δ_i through

$$\begin{aligned} m_{i,A} &= 2.5\log_{10}(1+10^{0.4\Delta_i}) + \mathcal{T}_i \\ m_{i,B} &= \Delta_i + m_{i,A}. \end{aligned} \tag{1}$$

Equation (1) gives three NIR apparent magnitudes for each star. These six NIR photometric measurements can be related to the stellar masses (M_A, M_B) through the following equation:

$$m_i(M,d) = \mathcal{M}_i(M) + 5(\log_{10} d - 1). \tag{2}$$

The functions $\mathcal{M}_i(M)$ give the absolute magnitudes in the NIR bands as a function of stellar mass, M, as determined by inversion of the empirical relationships of Delfosse et al. (2000), which we approximate with the polynomial

$$\mathcal{M}_i(M) = \sum_{j=0}^{5} b_{i,j} M^j. \tag{3}$$

Table 3
Polynomial Coefficients for Magnitude–Mass and Mass–Radius Relationships

j	b_J	b_H	b_{K_S}	b_V	b_R
0	14.888	13.211	13.454	−9.229	0.000
1	−74.375	−57.464	−67.439	5.017	1.268
2	376.72	271.11	338.43	−0.6609	−1.013
3	−1089.6	−762.12	−976.27	0.03314	0.9391
4	1601.6	1103.9	1433.9	...	...
5	−935.37	−640.80	−838.03	...	...

The coefficients $\{b_i\}$ are listed in Table 3 for the $i = \{J, H, K_S\}$ bands.

Under the assumption that the binary components share the same chemical composition, they should reside at the same distance from the average main sequence in the $\{V-K_S, M_{K_S}\}$ plane (Johnson & Apps 2009, hereafter JA09). JA09 provide a relationship between a star's metallicity, [Fe/H] $\equiv F$, and its "height" above the solar-neighborhood mean main sequence, ΔM_K. Since the stars share the same composition they must lie on the same isometallicity contour: their $V-K_S$ colors must be consistent with the same value of ΔM_K, while the individual V-band luminosities must be consistent with the measured $V_{\rm tot}$. This constraint can be expressed as

$$\begin{aligned} V_{\rm tot}(M_A, M_B, d, F) = {} & \mathcal{M}_{\rm V}(M_A, F) \\ & - 2.5\log_{10}(1+10^{0.4[\mathcal{M}_{\rm V}(M_A,F)-\mathcal{M}_{\rm V}(M_B,F)]}) \\ & + 5\log_{10} d - 5, \end{aligned} \tag{4}$$

where the absolute V-band magnitude, $\mathcal{M}_{\rm V}(M, F)$, is related to stellar mass M and metallicity F by inverting the photometric metallicity calibration of JA09.[9] We approximate this inversion using the polynomial

$$\mathcal{M}_{\rm V}(M,F) = \sum_{j=0}^{3} b_{\rm V,j}\left[\mathcal{M}_{K_S}(M) + \left(\frac{F-0.05}{0.55}\right)\right]^j. \tag{5}$$

The coefficients $\{b_V\}$ are listed in Table 3.

In addition to the apparent magnitudes, the transit light curve provides an additional constraint on M_A through the scaled semimajor axis $a/R_A \equiv a_R$. This quantity is related to the mass and radius of Star A, and the period and mass of LHS 6343 C, through

$$a_R(M_A, M_C, P) = \left(\frac{G}{4\pi^2}\right)^{1/3} \frac{M_A^{1/3}}{R_A(M_A)} P^{2/3}\left(1+\frac{M_C}{M_A}\right)^{1/3}, \tag{6}$$

[9] We use the JA09 relationship rather than the Schlaufman & Laughlin (2010, SL10) calibration because the former provides a better match to the mean metallicity of the solar neighborhood. In principle, the SL10 relationship would serve our purposes just as well since both V-band metallicity relationships provide a means of relating $V_{\rm tot}$ to the stellar masses under the constraint that both stars lie on the same isometallicity contour in the $\{V-K_S, M_{K_S}\}$ plane. The only difference is the exact value of [Fe/H], which will be ≈ 0.1 dex lower using the SL10 calibration.

where $R_A(M)$ is a function relating the stellar radius and mass. We use a polynomial fit to the masses and radii of well-characterized ($\{\sigma_M, \sigma_R\} < 3\%$) low-mass eclipsing binaries tabulated by Ribas (2006):

$$R_A(M) = \sum_{j=0}^{3} b_{R,j} M^j. \quad (7)$$

The coefficients $\{b_R\}$ are listed in Table 3.

The optimal stellar parameters can be obtained by minimizing the fitting statistic

$$\chi^2_{\rm tot} = \sum_{i=1}^{3} \left(\frac{m_{i,A} - m_i(M_A, d)}{\sigma_{m_{i,A}}} \right)^2 + \sum_{i=1}^{3} \left(\frac{m_{i,B} - m_i(M_B, d)}{\sigma_{m_{i,B}}} \right)^2 + \left(\frac{V_{\rm tot} - V_{\rm tot}(M_A, M_B, d, F)}{\sigma_{V_{\rm tot}}} \right)^2 + \left(\frac{a_R - a_R(M_A, M_C, P)}{\sigma_{a_R}} \right)^2. \quad (8)$$

However, we must account for the flux contribution of Star B to properly model the light curve and recover the true value of a_R. We describe this process in the following section.

5.2. Flux Contribution of Star B

Since both stars fall within the *Kepler* and Nickel photometric aperture, we must estimate the flux contribution of Star B in both the K_P and Z bandpasses. The transformation between the Johnson B and V magnitudes and the Kepler magnitude K_P is given in the Kepler Guest Observer Web site[10]. However, we note that this transformation is only given down to spectral type M0, and we were therefore forced to extrapolate to ~M2. To account for potential systematic errors related to this extrapolation, we inflate our measurement uncertainties for the calculated K_P magnitudes.

While we were able to measure individual V magnitudes for both stars based on their total V magnitude and derived physical properties using Equation (5), there is no suitable relationship between the available observables and the individual B magnitudes. We are therefore forced to rely on stellar model grids to estimate the $B-V$ colors of Stars A and B.

For this task, we selected the "Basic Set" of stellar model grids from the Padova group for solar composition and an age of 5 Gyr (Girardi et al. 2002), which give predictions for the Johnson B and V magnitudes as a function of stellar mass. We selected the Padova models because the Baraffe et al. (1998) model grids do not give fluxes in the B or Z bandpasses. We tested the reliability of the Padova model grids using a sample of six metal-rich stars from Johnson & Apps (2009). We found that the models underpredict the $B-V$ colors of our calibration stars by 0.20 ± 0.07, independent of stellar mass over a range of approximately 0.1–0.6 $M_\odot$. We applied this correction to the Padova models to obtain a refined relationship between stellar mass and $B-V$ color, and the uncertainty of this offset was folded into the final uncertainties in the colors.

[10] http://keplergo.arc.nasa.gov/CalibrationZeropoint.shtml

Using the estimates of the $B-V$ colors of Star A and Star B, together with the individual V-band magnitudes from Equation (5), we can estimate the relative magnitudes of the stars in the *Kepler* bandpass, ΔK_P, as a function of the stellar masses. We then use this value of ΔK_P to correct the *Kepler* light curve parameters. For the Nickel light curve, we use the SDSS z-band magnitude from the Padova model as a proxy for the Gunn Z filter.

Our reliance on low-mass stellar model grids for the magnitude differences is less than ideal, particularly in optical bandpasses, because of the difficulty in properly treating molecular opacities at optical wavelengths (e.g., Baraffe et al. 1998). In the analysis that follows, we attempt to ameliorate this imperfect knowledge by using large uncertainties for ΔK_P and ΔZ, which are propagated throughout our analysis and reflected in the confidence intervals for our derived system properties. We discuss the impact of our model-based magnitude differences in Section 6.2.

5.3. Light Curve Analysis

We fitted the *Kepler* and Nickel light curves using the analytic eclipse model of Mandel & Agol (2002) to compute the integrated flux from the uneclipsed stellar surface as a function of the relative positions of the star and planet. The parameters were the period P, inclination i, ratio of the companion and stellar radii R_C/R_A, the scaled semimajor axis a_R, time of mid-transit $T_{\rm mid}$, and the parameters describing the limb darkening of the star. For the limb darkening, we used the quadratic approximations of Sing (2010) and Claret (2004) for the *Kepler* and Z bands, respectively. In our model, we fixed the quadratic terms u_2 at the tabulated values for each filter, and allowed the linear term u_1 to vary under a penalty of the form $\exp[-(x-\mu_x^2)/\sigma_x^2]$, which is added to the fitting statistic. This treatment of the limb darkening was made based on the additional structure seen in the residuals of the *Kepler* light curve fit. Allowing the limb-darkening parameters to float freely results in unphysical values.

To properly model the light curves, we made two modifications to the typical light curve analysis. First, we corrected for the third-light component by adjusting the normalized flux level from the Mandel & Agol light curve model, $f_{\rm mod}$, such that

$$f_{\rm corr} = \frac{f_{\rm mod} + 10^{-0.4\Delta K_P}}{1 + 10^{-0.4\Delta K_P}}. \quad (9)$$

In our fitting procedure, we treat ΔK_P as a free parameter under the normally distributed, prior constraint $\mathcal{N}(\Delta K_P, \sigma_{K_P})$ based on the estimate of the magnitude differences described in Section 5.2. We use a similar prescription for the flux contribution of Star B to the Nickel Z bandpass. Our other modification involved rebinning the analytic light curve to match the 29.4 minute cadence of the data using a method similar to that of Kipping (2010).

In addition to modeling the companion transit, we also fitted a slowly varying function to the out-of-transit portion of the Nickel light curve to account for differential extinction from Earth's atmosphere. To account for time-correlated noise in the data, we used a Daubechies fourth-order wavelet decomposition likelihood function following the technique described by Carter & Winn (2009). Wavelet decomposition provides increased confidence in the derived parameter uncertainties over the traditional χ^2 likelihood by allowing parameters that measure photometric scatter (uncorrelated white noise σ_w, and $1/f$ red

noise σ_r) to evolve as free parameters. The method recovers the traditional χ^2 fitting statistic in the case of $\sigma_r = 0$, and when σ_w is fixed at a value equal to the characteristic measurement error.

We determined the best-fitting model parameters and their uncertainties using a Markov Chain Monte Carlo analysis with a Gibbs Sampler (Geman & Geman 1984; Ford 2005; Winn et al. 2009). The MCMC fitting algorithm was implemented using the Transit Analysis Package (Gazak et al. 2011), a graphical user interface-driven analysis tool written in the IDL. We constructed 10 chains containing 10^6 links using initial conditions based on a simple least-squares fit to the phased photometry. We chose step sizes such that 30%–40% of the steps are accepted. We discarded the initial 10^5 links in each parameter chain to allow for "burn-in" before combining the chains. The resulting chains of parameters form the posterior probability distribution, from which we select the 15.9 and 84.1 percentile levels in the cumulative distributions as the "1σ" confidence limits. In most cases, the posterior probability distributions were approximately Gaussian, and we therefore report only symmetric error bars for simplicity. The final, iterative fitting procedure and derived parameters are presented in Section 6.

6. PHYSICAL PROPERTIES OF THE LHS 6343 STELLAR SYSTEM

We solve for the physical parameters of the LHS 6343 system using the following iterative procedure.

1. Fit the light curves to obtain the scaled semimajor axis, a_R. We initially use $\Delta K_p = 0.7$, $\sigma_{K_P} = 0.1$, $\Delta Z = 0.5$, and $\sigma_Z = 0.1$ in Equation (9) and refine these values with subsequent iterations.
2. Estimate M_C based on our Keplerian fit to the RV time series by solving

$$M_C^3 \sin^3 i = \frac{K^3 P}{2\pi G}(M_A + M_C)^2\sqrt{1-e^2}. \quad (10)$$

   We initially assume $M_C \ll M_B$, and relax this assumption as M_A is revised.
3. Use a_R and M_C to estimate M_A and M_B by minimizing Equation (8).
4. Test for convergence in M_A, M_B, M_C, ΔK_P, and ΔZ by comparing the current values to those of the previous iteration. If the change is larger than 10% of the parameter uncertainties, then go to step 1.

We find that convergence is rapid, requiring only three iterations.

Our best-fitting stellar parameters are $M_A = 0.370 \pm 0.009$ $M_\odot$, $M_B = 0.30 \pm 0.01$ $M_\odot$, $d = 36.6 \pm 1.1$ pc, and [Fe/H] $= 0.04 \pm 0.08$. The fit results in $\chi^2_{\rm tot} = 2.1$ as defined in Equation (8), with eight data points and four free parameters (M_A, M_B, d, and [Fe/H]), indicating that our fit is acceptable but that our photometric measurement uncertainties given in Table 1 are likely overestimated. The best-fitting model values are compared to the observed quantities in Figure 4. The marginalized, posterior probability density functions (pdfs) are shown in Figure 5.

Our analysis of the light curve results in $R_C/R_A = 0.226 \pm 0.003$ and $a_R = 45.3 \pm 0.6$, with $\Delta K_P = 0.74 \pm 0.10$ and $\Delta Z = 0.5 \pm 0.1$. The best-fitting transit model is shown in Figure 1 for both the *Kepler* (blue) and Nickel data (red), along with the residuals. For both data sets we recover $\sigma_r = 0$, consistent with no red noise contamination. However, we do see additional structure in the in-transit residuals of the *Kepler* fit. We do not know the source of this increased scatter. Because there are so few points, and because the data do not appear to be time-correlated during any single transit event, we found that the extra scatter is accounted for by allowing the fitting procedure to increase the white-noise component, σ_w. We find $\sigma_w = 1.1 \times 10^{-3}$ (1.8 minute cadence) for the Nickel data and $\sigma_w = 1.1 \times 10^{-4}$ (29.4 minute cadence) for the *Kepler* data.

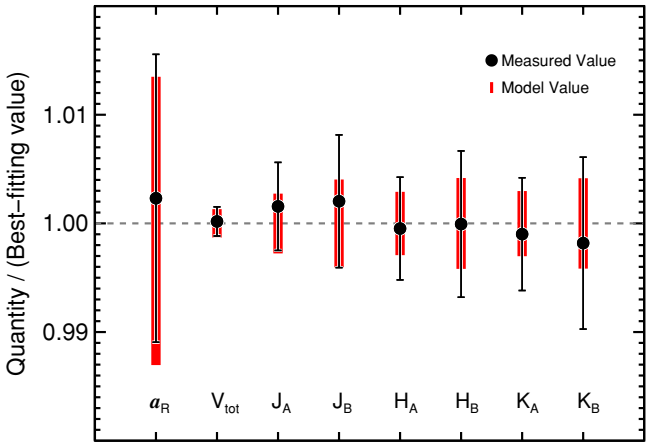

Figure 4. Comparison of the observed photometric and transit properties (filled circles with error bars) and the corresponding quantities predicted by our model (red swaths; Equations (2), (4), and (6)). In order to show all parameters on the same scale, the quantities have been divided by the best-fitting model values. The widths of the red swaths indicate the range of values explored by our fitting analysis.

(A color version of this figure is available in the online journal.)

6.1. The Radii of LHS 6343 A and LHS 6343 C

Given the mass of Star A, we can estimate the stellar radius by evaluating Equation (7) which results in a stellar radius $R_A = 0.378 \pm 0.008$ $R_\odot$. The radius ratio from the light curve analysis, together with R_A yields the radius of LHS 6343 C, $R_C = 0.833 \pm 0.021$ $R_{\rm Jup}$. The other physical properties of the brown dwarf are listed in Table 5.

6.2. The Dependence of R_C on the Flux Contribution of LHS 6343 B

In Section 5.2, we describe our method of estimating the flux contribution of Star B, as parameterized by the magnitude differences ΔK_P and ΔZ. These values are of central importance to the determination of the true values of a/R_A and R_C/R_A as derived from the analysis of the light curves, and hence the physical properties of the brown dwarf. Unfortunately, we do not have spatially resolved photometry of the binary stars, so we were forced to rely on theoretical stellar models to estimate the magnitude differences. Owing to incomplete knowledge of molecular opacities, particularly in optical bandpasses, the model grids provide only rough estimates of the true flux contribution of Star B. To encapsulate this imperfect knowledge in our analysis, we used relatively large uncertainties (0.1 mag) for ΔK_P and ΔZ. These errors are propagated throughout our MCMC analysis and are reflected in the final physical properties of the LHS 6343 system.

As a test, we performed independent fits to the *Kepler* and *Z*-band light curves. We found that the transit properties from the two analyses agreed extremely well, differing by only a fraction of a σ in each value. Figure 6 illustrates the dependence of R_C on ΔK_P and ΔZ, and compares the value of R_C measured

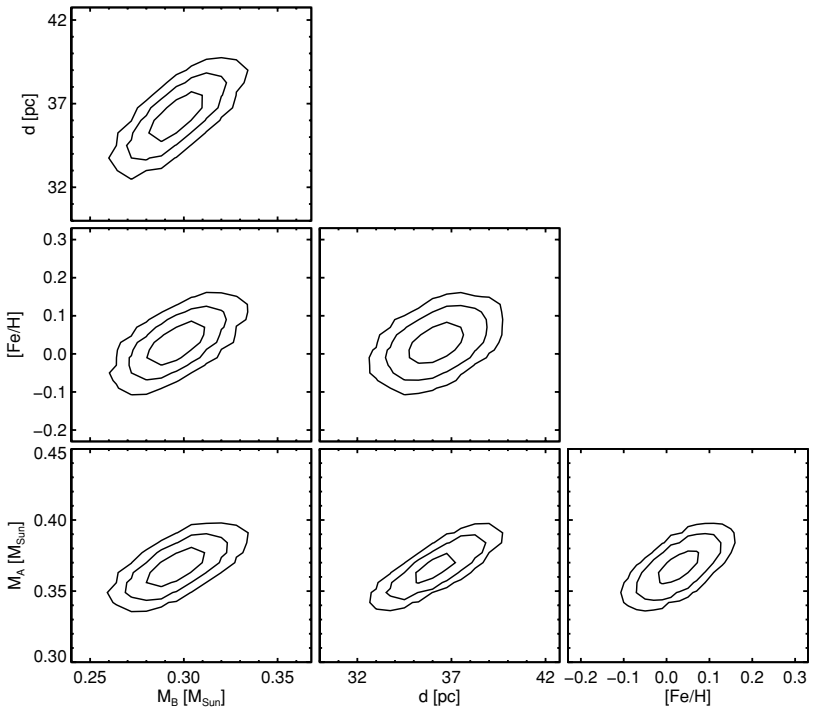

Figure 5. Each panel shows the joint, posterior pdfs for two parameters at a time, marginalized over the remaining parameters. The contours show the iso-probability levels corresponding to {68.2, 95, 99.7}% confidence.

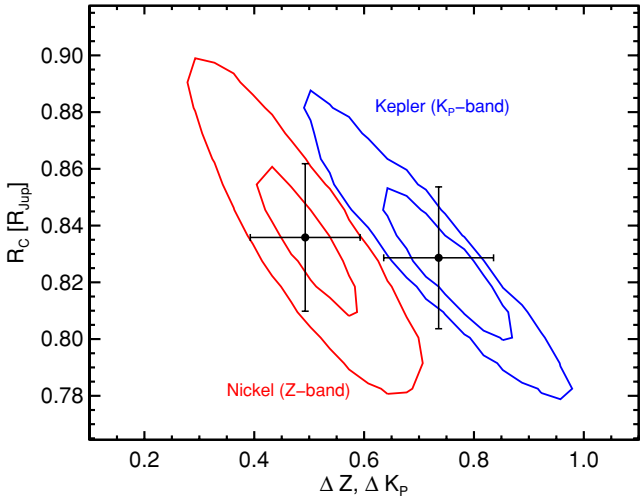

Figure 6. Dependence of R_C on ΔK_P (upper, blue) and ΔZ (lower, red), based on the marginalized posterior pdfs. The contours represent the 68.2% and 95% confidence regions. The two filled circles with error bars show the final values of R_C, ΔK_P, and ΔZ from our analysis, and the error bars represent the corresponding 68.2% confidence bounds in each dimension.

(A color version of this figure is available in the online journal.)

from the independent light curve fits. Based on this figure, we feel that our value of ΔZ is reasonable since its value should not be less than $\Delta J = 0.49$. Similarly, ΔZ should not exceed our estimate of ΔK_P, and ΔK_P should not be much larger than our measured $\Delta V = 0.74$. These results, along with the close agreement between the two measurements of R_C, provide additional confidence that our model-based magnitude differences are valid.

6.3. Searching for Transit Timing Variations

To measure the individual transit mid-times, we fixed all of the global parameters (R_C/R_A, a/R_A, P, i, and the limb-darkening coefficients) and fitted each transit event separately using the MCMC algorithm described in Section 5.3. Table 4 lists the time at the mid-point of each transit $T_{\rm mid}$; the difference between the measured values and the those predicted by a linear ephemeris; and the formal measurement uncertainties which range from 10 to 23 s. We see no statistically significant timing variations.

Table 4
LHS 6343 Ephemeris

$T_{\rm mid}$ (BJD–2450000.0)	$T_{\rm mid}$–Ephemeris	Telescope
4957.216636 ± 0.000073	0.0000020 ± 0.00012	K
4969.930410 ± 0.000099	0.000045 ± 0.00014	K
4982.64437 ± 0.00013	0.000093 ± 0.00016	K
4995.35807 ± 0.00015	0.000028 ± 0.00018	K
5376.77274 ± 0.00025	0.0000050 ± 0.00027	N

Note. K: *Kepler*; N: Nickel *Z* band.

6.4. Limits on the Secondary Eclipse Depth

To place an upper limit on the secondary eclipse depth, we fitted a simplified transit model to the *Kepler* photometry near one-half phase away from the primary eclipse. We held constant the transit parameters from the fit to the primary eclipse, along with e and ω the from the RV analysis; assumed no limb darkening; and used final value of $\Delta K_P = 0.74 \pm 0.10$. By allowing only the transit depth, σ_w and the terms describing the out-of-transit normalization to vary, we place a 95% upper limit on the eclipse depth of $d < 6.5 \times 10^{-5}$.

6.5. Limits on the System Age

Measuring the ages of M-type stars is notoriously difficult, except for the rare cases when stars are in clusters or associations, or show indications of extreme youth. The space motion of LHS 6343 rules out membership in any known moving group or cluster. We therefore must rely on spectroscopic and

Table 5
System Parameters of LHS 6343

Parameter	Value	68.3% Confidence Interval	Comment
Transit parameters			
Orbital period, P (days)	12.71382	±0.00004	A
Radius ratio, $(R_C/R_{\star,A})_{\rm corr}$	0.226	±0.003	A
Transit depth, $(R_C/R_{\star,A})^2_{\rm corr}$	0.051	±0.001	A
Scaled semimajor axis, $a_R \equiv a/R_\star$	45.3	±0.6	A
Orbit inclination, i (deg)	89.50	±0.05	A
Transit impact parameter, b	0.40	±0.04	A
Other orbital parameters			
Semimajor axis between Stars A and C (AU)	0.0804	±0.0006	B
Eccentricity	0.056	±0.032	C
Argument of periastron, ω (deg)	−23	±56	C
Velocity semiamplitude, K_A (km s^{-1})	9.6	±0.3	C
Systemic radial velocity, γ (km s^{-1})	−46.0	±0.2	C
Stellar parameters			
M_A ($M_\odot$)	0.370	±0.009	D
M_B ($M_\odot$)	0.30	±0.01	D
$R_{\star,A}$ ($R_\odot$)	0.378	±0.008	D
ρ_A ($\rho_\odot$)	6.6	±0.5	A
$\log g_A$ (cgs)	4.851	±0.008	B
[Fe/H]	0.04	±0.08	D
Distance (pc)	36.6	±1.1	D
V_A (mag)	13.88	±0.03	E
V_B (mag)	14.63	±0.06	E
$(B-V)_A$	1.57	±0.07	F,G
$(B-V)_B$	1.60	±0.07	F,G
ΔK_P (mag)	0.74	±0.10	F
ΔZ (mag)	0.5	±0.1	F,G
$T_{{\rm eff},A}$ (K)	3130	±20	H
$T_{{\rm eff},B}$ (K)	3030	±30	H
Brown dwarf parameters			
M_C ($M_{\rm Jup}$)	62.7	±2.4	B,C
R_C ($R_{\rm Jup}$)	0.833	±0.021	B
Mean density, ρ_C (g cm^{-3})	109	±8	B,C
$\log g_C$ (cgs)	5.35	±0.02	A

Notes. (A) Determined from the parametric fit to the *Kepler* light curve. (B) Based on group A parameters supplemented by the photometric stellar mass determination described in Section 5. (C) Based on our analysis of the Keck/HIRES RV measurements. (D) Based on our photometric mass and radius determinations described in Section 5. (E) Equation (5). (F) Interpolation of Padova model grids. (G) $(B-V)$ colors from the Padova models have been corrected by adding empirically measured offset of 0.21 ± 0.07 mag. Gunn-Z magnitudes were approximated using SDSS z'-band, with an additive correction of 0.07 mag based on the difference between the model ΔJ compared to the measured ΔJ in Table 1. (H) Based on the $V - K_S$ effective temperature calibration of Casagrande et al. (2008).

kinematic indicators that can at least tell us if a star is either younger or older than a few Gyr.

Our HIRES spectra show no lithium absorption, no Hα emission, and remarkably low chromospheric activity in the Ca II K line (Figure 7). None of the 140 low-mass stars on the CPS M dwarf survey have chromospheric S values, as measured on the Mt. Wilson scale (Wright et al. 2004), as low as what we measure for LHS 6343 A. After attempting to correct for the ≈30% contamination from Star B to the emission core, we estimate $S \approx 0.4$ for LHS 6343 A. The most chromospherically quite M dwarf in the CPS sample is Gl 445, with an average of $S = 0.5$.

LHS 6343 was not detected by *ROSAT*,[11] but at 36.6 pc this only rules out extremely young ages less than ∼100 Myr. Our HIRES spectra exhibit narrow lines indicating $V_{\rm rot} \sin i <$ 2 km s^{-1}. Thus, the age of the LHS 6343 system is most likely greater than 1–2 Gyr.

7. DISCUSSION

LHS 6343,C is remarkably similar to the brown dwarf NLTT41135 B, recently discovered by the *MEarth* transit survey (Irwin et al. 2010). Both brown dwarfs orbit one component of a nearby M+M visual binary, both stellar systems are hierarchical triples, and both were discovered through transit photometry. However, owing to its more favorable orbital inclination, transit photometry provides a direct measurement of the radius LHS 6343 C.

The large mass ratio between parent star and companion argues against the formation of LHS 6343 C in the protoplanetary disk of LHS 6343 A. This is because there is likely not enough material in the disks of M dwarfs to build a 62.7 $M_{\rm Jup}$ companion, whether through core accretion (Laughlin et al. 2004)

[11] The *Rontgensatellit* (*ROSAT*) was a joint German, US, and British X-ray observatory operational from 1990 to 1999.

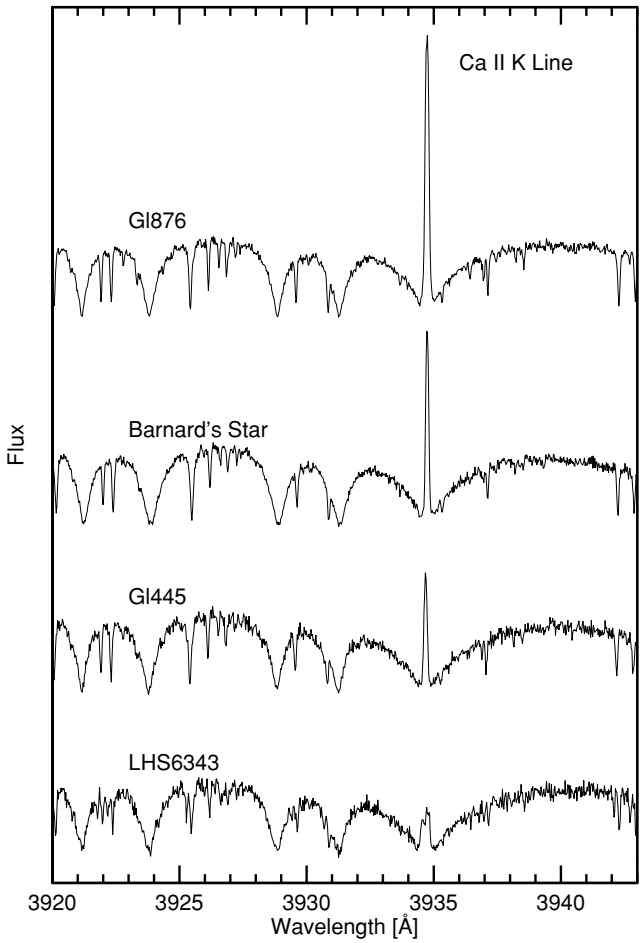

Figure 7. HIRES spectra near the Ca II K line for LHS 6343 and several M dwarfs with ages greater than 1 Gyr.

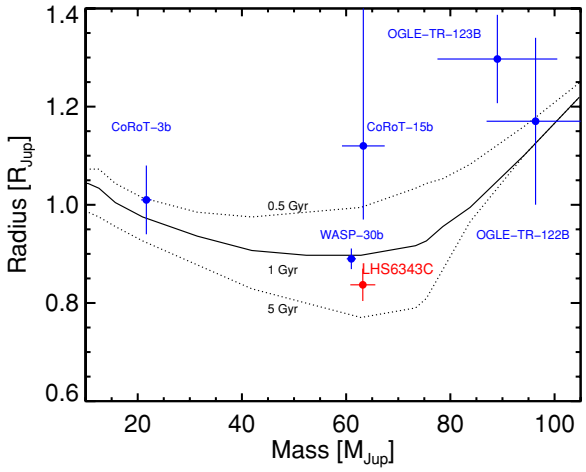

Figure 8. Masses and radii of known low-mass, transiting objects. Also plotted are the predicted mass–radius curves from the Baraffe et al. (1998) interior structure models for 0.5, 1, and 5 Gyr, top to bottom, and solar metallicity. Not shown are the young, eclipsing brown dwarfs in the 2MASS 2053-05 system (Stassun et al. 2006), which have radii well above the plot range.

(A color version of this figure is available in the online journal.)

or disk instability (Boss 2006). It is therefore more likely that LHS 6343 C formed in a similar manner as LHS 6343 B, through the fragmentation of a portion of their natal molecular cloud. Irwin et al. (2010) make similar arguments regarding the origin of NLTT 41135 B.

Prior to this year, the only other brown dwarfs with accurate radius measurements were the substellar components of the 2MASS J05352184-0546085 EB system (Stassun et al. 2006), and CoRoT-3 b (Deleuil et al. 2008). The 2MASS J05352184-0546085 system was discovered in a young star-forming region, and the two brown dwarfs have very large radii for their masses (0.669 $R_\odot$ and 0.611 $R_\odot$) because they are still undergoing gravitational collapse.

In the latter portion of this year, two other transiting field brown dwarfs have been discovered by transit surveys. The ground-based Wide Angle Survey for Planets discovered WASP-30 b (60.96 ± 0.89 $M_{\rm Jup}$, 0.89 ± 0.21 $R_{\rm Jup}$; Anderson et al. 2011), and the space-borne *CoRoT* mission discovered CoRoT-15 b (63.3 ± 1.1 $M_{\rm Jup}$, $1.12^{+0.3}_{-0.15}$ $R_{\rm Jup}$; Bouchy et al. 2011). Both of these companions have masses comparable to LHS 6343 C, yet orbit single, F-type stars that are much more massive than LHS 6343 A. The current sample of known transiting brown dwarfs are shown in Figure 8, along with two very low mass eclipsing M dwarfs. Also shown are the mass and radius predictions of the Baraffe et al. (1998) interior models for three different ages, illustrating that the radius of LHS 6343 C is consistent with the model predictions for a brown dwarf with an age >1 Gyr yet <5 Gyr.

Our knowledge of the physical characteristics of brown dwarfs is starting to expand owing to the growing productivity and efficiency of wide-field transit surveys, both from the ground and in space. LHS 6343 is one of the closest stars in the *Kepler* field and points the way toward additional brown dwarf discoveries in the near future.

We thank Keivan Stassun and Leslie Hebb for providing us with their *B* and *V* photometry of the LHS 6343 system. We thank Jonathan Irwin for his independent analysis of the *Kepler* light curve and for encouraging us to incorporate the third-light correction into our forward-modeling procedure; Josh Carter for independently confirming our best-fitting light curve parameters; and John Gizis for pointing out an error in our calculation of the brown dwarf mass in an earlier draft of this manuscript. We gratefully acknowledge the tireless dedication and hard work of the *Kepler* team, without whom this project would not be possible. In particular, we thank Jon Jenkins and Lucianne Walkowicz for confirming the planet-like nature of the transits following the initial identification of transit events by K.A. We gratefully acknowledge the efforts and dedication of the Keck Observatory staff, especially Grant Hill, Scott Dahm, and Hien Tran for their support of HIRES and Greg Wirth for support of remote observing. We made use of the SIMBAD database operated at CDS, Strasbourge, France, and NASA's Astrophysics Data System Bibliographic Services. A.W.H. gratefully acknowledges support from a Townes Post-doctoral Fellowship at the U.C. Berkeley Space Sciences Laboratory. G.W.M. acknowledges NASA grant NNX06AH52G. Finally, we extend special thanks to those of Hawaiian ancestry on whose sacred mountain of Mauna Kea we are privileged to be guests. Without their generous hospitality, the Keck observations presented herein would not have been possible.

REFERENCES

Allard, F., et al. 2001, ApJ, 556, 357
Anderson, D. R., et al. 2011, ApJ, 726, L19
Baraffe, I., et al. 1998, A&A, 337, 403
Basri, G. 2006, Astron. Nachr., 327, 3
Basri, G., Marcy, G. W., & Graham, J. R. 1996, ApJ, 458, 600

Batalha, N. M., et al. 2010, ApJ, 713, L109
Borucki, W. J., et al. 2010, Science, 327, 977
Boss, A. P. 2006, ApJ, 643, 501
Bouchy, F., et al. 2011, A&A, 525, A68
Bowler, B. P., Liu, M. C., & Cushing, M. C. 2009, ApJ, 706, 1114
Burgasser, A. J., et al. 1999, ApJ, 522, L65
Burgasser, A. J., et al. 2007, in Protostars and Planets V, ed. B. Reipurth, D. Jewitt, & K. Keil (Tucson, AZ: Univ. Arizona Press), 427
Burrows, A., et al. 1997, ApJ, 491, 856
Carter, J. A., & Winn, J. N. 2009, ApJ, 704, 51
Casagrande, L., Flynn, C., & Bessell, M. 2008, MNRAS, 389, 585
Charbonneau, D., et al. 2005, ApJ, 626, 523
Chubak, C., & Marcy, G. 2011, BAAS, 43, 434.12
Claret, A. 2004, A&A, 428, 1001
Cushing, M. C., & Vacca, W. D. 2006, AJ, 131, 1797
Deleuil, M., et al. 2008, A&A, 491, 889
Delfosse, X., et al. 2000, A&A, 364, 217
Delorme, P., et al. 2008, A&A, 484, 469
Droege, T. F., et al. 2006, PASP, 118, 1666
Eastman, J., Siverd, R., & Gaudi, B. S. 2010, PASP, 122, 935
Fischer, D. A., & Valenti, J. 2005, ApJ, 622, 1102
Ford, E. B. 2005, AJ, 129, 1706
Gary, B. L. 2007, in Society for Astronomical Sciences Annual Symp., Vol. 26, ed. B. D. Warner et al. (Rancho Cucamonga, CA: SAS), 23
Gazak, J. Z., Johnson, J. A., Tonry, J., Eastman, J., Mann, A. W., & Agol, E. 2011, arXiv:1102.1036
Geman, S., & Geman, D. 1984, IEEE Trans. Pattern Anal. Mach. Intell., 6, 721
Girardi, L., et al. 2002, A&A, 391, 195
Grether, D., & Lineweaver, C. H. 2006, ApJ, 640, 1051
Hayward, T. L., et al. 2001, PASP, 113, 105
Howard, A. W., et al. 2010, ApJ, 721, 1467
Irwin, J., et al. 2010, ApJ, 718, 1353
Jenkins, J. M., et al. 2010a, ApJ, 724, 1108
Jenkins, J. M., et al. 2010b, ApJ, 713, L87
Jenkins, J. M., et al. 2010c, ApJ, 713, L120
Johnson, J. A. 2009, PASP, 121, 309
Johnson, J. A., & Apps, K. 2009, ApJ, 699, 933
Johnson, J. A., et al. 2004, AJ, 128, 1265
Johnson, J. A., et al. 2008, ApJ, 686, 649
Johnson, J. A., et al. 2010, PASP, 122, 905
Kipping, D. M. 2010, MNRAS, 408, 1758
Koch, D. G., et al. 2010, ApJ, 713, L79
Kratter, K. M., Murray-Clay, R. A., & Youdin, A. N. 2010, ApJ, 710, 1375
Landolt, A. U. 1992, AJ, 104, 340
Laughlin, G., Bodenheimer, P., & Adams, F. C. 2004, ApJ, 612, L73
Lawrence, A., et al. 2007, MNRAS, 379, 1599
Liu, M. C., Dupuy, T. J., & Ireland, M. J. 2008, ApJ, 689, 436
Liu, M. C., & Leggett, S. K. 2005, ApJ, 634, 616
López-Morales, M. 2007, ApJ, 660, 732
Mandel, K., & Agol, E. 2002, ApJ, 580, L171
Maness, H. L., et al. 2007, PASP, 119, 90
Marcy, G. W., & Butler, R. P. 2000, PASP, 112, 137
Martin, E. L., et al. 1997, A&A, 327, L29
McCarthy, C., & Zuckerman, B. 2004, AJ, 127, 2871
Oppenheimer, B. R., et al. 1995, Science, 270, 1478
Reid, I. N., et al. 2004, AJ, 128, 463
Ribas, I. 2006, Ap&SS, 304, 89
Schlaufman, K. C., & Laughlin, G. 2010, A&A, 519, A105
Seager, S., & Mallén-Ornelas, G. 2003, ApJ, 585, 1038
Sing, D. K. 2010, A&A, 510, A21
Sozzetti, A., et al. 2007, ApJ, 664, 1190
Stassun, K. G., Mathieu, R. D., & Valenti, J. A. 2006, Nature, 440, 311
Torres, G. 2007, ApJ, 654, 1095
Torres, G., Winn, J. N., & Holman, M. J. 2008, ApJ, 677, 1324
Troy, M., et al. 2000, Proc. SPIE, 4007, 31
Winn, J. N. 2008, in ASP Conf. Ser. 398, Extreme Solar Systems, ed. D. Fischer et al. (San Francisco, CA: ASP), 101
Winn, J. N., et al. 2009, ApJ, 693, 794
Wright, J. T., & Howard, A. W. 2009, ApJS, 182, 205
Wright, J. T., et al. 2004, ApJS, 152, 261